A Novel Electric Vehicle for Smart Indoor Mobility

Andrea G. Bianchessi, Carlo Ongini, Ivo Boniolo, Giovanni Alli, Cristiano Spelta,
Mara Tanelli, *Senior Member, IEEE*, and Sergio M. Savaresi, *Senior Member, IEEE*

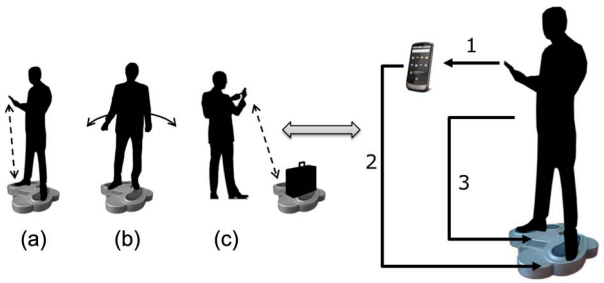

Fig. 1. (Left) Different ways to use the electric vehicle. The user controls the system with the smartphone (a) and (c) or by shifting the body weight (b). (Right) Possible user's interactions with the electric vehicle. Smartphone inertial and touch commands sent via Bluetooth (1) and feet commands (2) sent via pressure sensors (3) .

I. Introduction

DESIGNING effective personal mobility solutions for large indoor environments such as expositions, airports, hospitals, and warehouses is a challenging task. Standard automated systems such as treadmills, escalators, and elevators force the users to follow prearranged paths, whereas the current aim is that of devising new solutions that provide free movement in all directions. In this context, new vehicles have been proposed by major automotive companies: the well-known Segway [1]; the Honda U3-X, a unicycle with a foldable seat and footrests that is driven by the users' weight balance; and the Toyota Winglet, which has two wheels but no handlebars, so that it must constantly monitor the user's position to actively ensure stability. It is worth noting that an important requirement that must be met to fulfill the needs of the staff working in indoor environments is to provide vehicles that can be driven while leaving the rider's hands free to carry out activities efficiently. As a result, the most recent proposals have focused on the development of small-size vehicles that do not require the use of handlebars. As mentioned, the U3-X unicycle developed by Honda and the Toyota Winglet, both very recently launched (2008 and 2009, respectively), are the two most interesting prototypes conceived for personal indoor mobility. Both are small in size, electrically propelled, and do not have handlebars. The Winglet is a self-balancing two-wheeled scooter, very close in form and function to the Segway. On the Honda U3-X, which is without handlebars, too, each foot stands on its support, which resembles a pedal, and the user sits on it. Thus, the U3-X is essentially a motorized stool. Given these design choices, then, these two vehicles are not easy to drive, and usability is limited by the peculiar way in which the driver has to balance their weight.

The vehicle described herein was developed with these examples in mind and it aims to contribute to personal indoor mobility by providing a versatile and fully innovative solution designed for the transportation of a single passenger or small loads. This vehicle concept has been recently patented (see [2]). Specifically, the concept is an indoor vehicle constituted by a single platform on which the rider stands with both feet and which has no handlebars. Such vehicle can be safely driven, steered, and stopped based on the rider's posture, which is estimated by the pressure exerted on the sensors (see also [3]). This is the essential idea behind the patent, which was then further elaborated to comprise the driving mode based on the smartphone. Fig. 1 shows a pictorial overview of the whole system; to visually inspect the vehicle and its behavior, refer to the demo video that is available at http://youtube/PfyyNZlAMis.

With respect to the existing solutions mentioned, the aim of the proposed approach was to envision a smart, yet simple, vehicle mechanical layout that enables an easy management of the control systems needed to ensure free but safe movements, [4]. Specifically, the vehicle's motion is controlled by two independent electric motors with two double driving wheels that are mounted parallel and perpendicular to the longitudinal movements, respectively, [5], [6]. Furthermore, two additional castor wheels are added to ensure the balance of the system.

Manuscript received September 12, 2012; revised May 21, 2013, October 3, 2013, and December 9, 2013; accepted December 22, 2013. This work was supported in part by *Servizi per la Mobilitá Sostenibile*. The Associate Editor for this paper was X. Zhang.

A. G. Bianchessi, C. Ongini, G. Alli, M. Tanelli, and S. M. Savaresi are with the Dipartimento di Elettronica e Informazione, Politecnico di Milano, 20133 Milano, Italy (e-mail: gbianchessi@elet.polimi.it; ongini@elet.polimi.it; alli@elet.polimi.it; tanelli@elet.polimi.it; savaresi@elet.polimi.it).

I. Boniolo and C. Spelta are with the Dipartimento di Ingegneria dell' Informazione e metodi Matematici, Universitá degli Studi di Bergamo, 24044 Dalmine, Italy (e-mail: ivo.boniolo@unibg.it; cristiano.spelta@unibg.it).

Color versions of one or more of the figures in this paper are available online.

With such a setting, steering is just a matter of varying the speed of the driving wheels, the appropriate management of which is dealt with by means of appropriate control systems. In this respect, an appropriate choice of the controlled variables will allow us setting up a decoupled control problem, which can be effectively solved by linear and time invariant control loops ensuring good performance and safety. Note that the other existing vehicles, instead, rely on some form of the inverted-pendulum dynamics, thereby being rather sensitive to variations in the system parameters and needing accurate and complex control systems to correctly manage their motion. The other innovation enabled by the proposed vehicle is the combined driving mode, which comprises the use of a smartphone providing the needed inertial sensors to specify the user's intentions in terms of vehicle motion and the balancing of the rider's weight. An appropriate communication is defined between the smartphone and the vehicle system in order to coordinate the motion commands. In this respect, it is worth mentioning that recent work have presented smartphone-based interfaces to stabilize and drive quad-rotor vehicles (see, e.g., [7] and [8] and the references therein).

Moreover, the peculiar driving posture requested an ad hoc analysis of the related safety issues, leading to the design of specific automatic procedures to ensure a safe vehicle operation.

The outline of this paper is as follows. In Section II, a brief description of the prototype vehicle is presented, whereas Section III analyzes the riding commands. The vehicle kinematic and dynamic models are described in Section IV, leading to the definition of the model-based control problem, which is discussed in Section V. Finally, Section VI presents the vehicle supervisory unit that enforces the needed safety constraints.

II. Vehicle Description

The vehicle consists of a plastic chassis covered by a thin layer of nickel to strengthen the structure. The chassis basis has a metallic cover, which protects the mechanical and electronic components [see Fig. 2 (top right)]. Four wheels (two driving and two pivoting) ensure both stability and energy savings. Note, in fact, that the two most promising existing vehicles for indoor mobility (the U3-X and the Winglet), being based on an inverted-pendulum configuration, continuously need energy to ensure stability (see, e.g., [9]). While the vehicle is moving, the small size and the position of the wheels make an observer think that the vehicle is floating in the air. Indeed, all four wheels are well hidden within the chassis.

A liquid crystal display (LCD) screen is embedded between the two metal insoles present on the top on which the rider must position his feet [see Fig. 2 (top left)]. The 5.7-inch LCD device is used to convey information about the vehicle status to the user, displaying the vehicle speed, the distance covered, the battery pack state of charge, and some safety notifications (typically related to an unsafe feet posture, e.g., one foot is not placed over the corresponding insole).

Overall, the electronic and mechanical components of the considered vehicle are the following.

- Two 12-V dc motors with appropriate power-to-weight ratio. The maximum power is up to 200 W, and the weight is approximately 400 g. The motor torque of 110 mN · m is insufficient for the considered application, so that a reduction stage with a ratio of 5.33 was added.
- Two incremental encoders based on capacitive technology placed at the motor shafts. They provide the speed measurements needed for controlling the vehicle motion.
- Pressure sensors are used to generate steering commands and are based on resistive technology, ultrathin (0.203 mm), and extremely flexible to be easily integrated below the metal insoles. The sensors can measure up to 110 N over the sensor active area with a response time of less than 5 ms.
- A 185-Wh battery pack, made up of ten rechargeable lithium cells in a 5 serial and 2 parallel configuration and a nominal voltage of 18.5 V, has an estimated time range of more than 2 h (which is appropriate considering a typical driving session in a large indoor environment), and corresponds to a covered distance of approximately 10 km. The battery pack is equipped with an ad hoc battery management system (BMS), which monitors the state of every cell during charging and discharging phases.
- A Bluetooth module is used to connect the remote controller to the vehicle using the serial Bluetooth profile.
- A main electronic control unit (ECU) hosts the control loops for managing the vehicle motion control.

Fig. 2. (Top left) Front and (top right) back views of the vehicle. (Bottom left) Screen view of the dashboard. (Bottom right) Sreenshots of the smartphone application developed for controlling the vehicle.

All the electronic components are shown in Fig. 3, which shows a view of the vehicle without its metallic cover. The BMS, the main ECU, and the LCD screen are all connected to each other *via* a controller area network (CAN) bus.

The main ECU was specifically designed for this vehicle: it is a dual-core board based on two *Microchip dsPIC* microcontrollers, which read data from the pressure sensors and from the Bluetooth module and run the vehicle motion control algorithms. Specifically, the first microcontroller executes the control algorithms related to the differential drive system due to two *full H-bridges* that regulate the voltage at the motors'

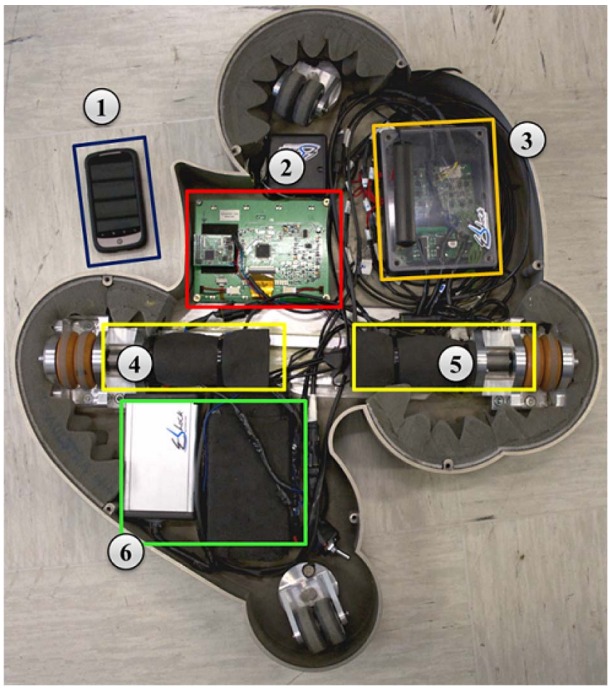

Fig. 3. Back view of the vehicle, which shows all electronic and mechanical components: ①—smartphone; ②—LCD controller; ③—ECU; ④ and ⑤—electric motors; ⑥—battery pack and BMS.

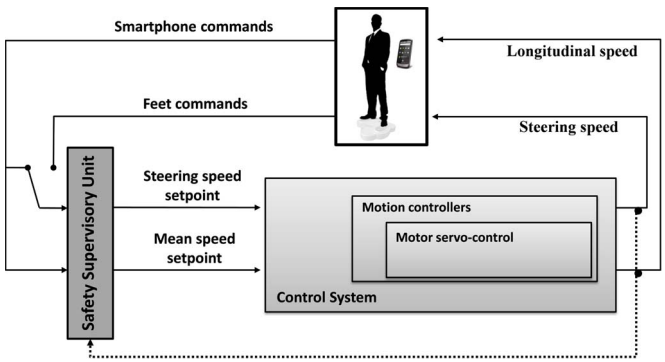

Fig. 4. High-level view of the control system.

terminals through *pulsewidth-modulation* (PWM) signals; whereas the second one processes the pressure sensors signals, receives commands from the smartphone *via* Bluetooth, and coordinates the communication among the different devices connected to the vehicle's CAN bus. Finally, the two microcontrollers are connected to each other *via* a serial bus.

Before being received by the microcontroller, the riding commands are sent to the *safety supervisory unit* (SSU), which ensures safe vehicle operations (see Section VI for more details). The commands are analyzed and possibly modified in order to avoid dangerous situations (e.g., too high steering speed and longitudinal acceleration requests; see Section VI) and then sent to the ECU, which actuates the two electric motors through two nested loops according to the control algorithms that will be described in Section V: an outer loop controls the longitudinal and steering speeds, whereas the inner one handles the servo control of the motor currents. Fig. 4 illustrates the high-level layout of the whole system.

TABLE I
COMPARISON BETWEEN THE SEGWAY AND THE PROPOSED VEHICLE

	Segway	**Proposed vehicle**
Weight	47-54 kg	12 kg
Handlebars	yes	no
Maximum speed	20 $\frac{km}{h}$	10 $\frac{km}{h}$
Energy consump. from wall outlet	32.5 $\frac{Wh}{km}$	37 $\frac{Wh}{km}$
Range	14-39 km	10 km
Charging time	8 h	3.5 h
Max. driver weight	117 kg	100 kg
Ground clearance	8.5-11.2 cm	1.5 cm

Finally, it is worth noting that moving from wired to wireless communications and using software applications that run on the users' smartphone, particularly in the electric vehicle fields, is one of the challenges in the coming years (see, e.g., [10]–[14] for different examples of the use and impact of smartphones in vehicle-based application and in transportation systems at large). For the considered vehicle, the smartphone constitutes the main interface between the vehicle itself and the rider: the connection takes place based on a Bluetooth channel and, due to the smartphone inertial sensors and the touchscreen, the user can control the vehicle direction, manage its settings and preferences, and select the desired driving mode. In addition, the smartphone and the two metal insoles on which the riders' feet are placed constitute the other innovative interface between the vehicle and the rider. Each of them hosts four pressure sensors, which are used to capture the rider's steering commands. The electronic hardware of the vehicle allows the user to drive it by the combined use of the smartphone and of the weight balance over the two plantars.

Remark 2.1 (Energy Efficiency and Comparison With the Segway): Energy efficiency is certainly an important aspect for the type of vehicles considered in this paper. In this respect, the Segway is the existing vehicle with which it is most interesting to compare our proposal, as it is mainly intended for indoor mobility and it has undergone a significant energy-oriented optimization of both its design and the motion-control algorithms. According to the data in [15], the main comparative terms between the two vehicles have been gathered and are reported in Table I. As can be seen, the Segway's energy consumption from a wall outlet is approximately 32.5 Wh/km, whereas that of the proposed vehicle is approximately 37 Wh/km (given by a 185-Wh battery, 50% efficiency in the recharging process, and 10 km of range). At the wheel, the vehicle's energy consumption is 18.5 Wh/km. Note that, as for the considered vehicle, no energy-oriented optimization of the control algorithms and of the vehicle management has been performed until now; the obtained energy efficiency is promising.

Remark 2.2 (Vehicle Limitations): The two main limitations of the proposed vehicle are the maximum speed value and the fact that it can be used only on flat floors. The first is due to the absence of the handlebars, which causes the vehicle to be unsafe for the rider at higher speeds. As a consequence, the speed has been limited to 10 km/h (which is adequate for indoor mobility). The second is due to the vehicle design, which causes the vehicle to have a 1.5-cm ground clearance, which is too small for outdoor mobility but optimal for large indoor exhibition spaces. As such, the motion limits indeed exist but are perfectly adequate for the intended application domain.

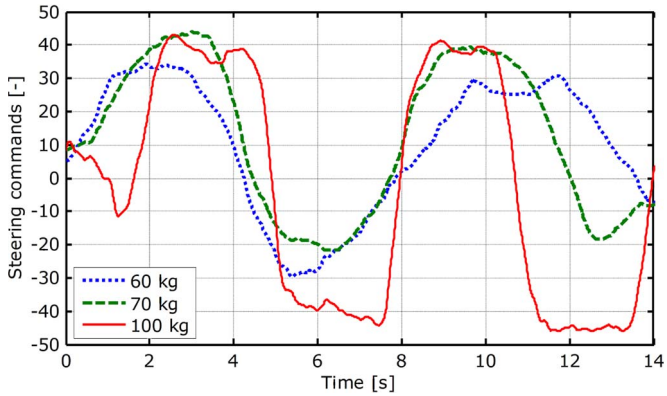

Fig. 5. Steering commands generated by different riders: (dotted line) 60 kg, (dashed line) 70 kg, and (solid line) 100 kg.

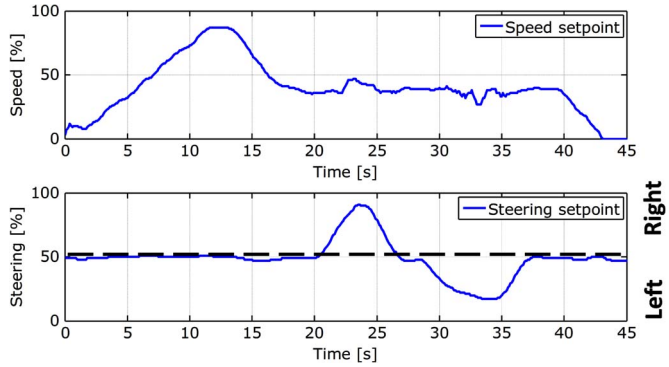

Fig. 6. Speed and steering commands generated using the smartphone.

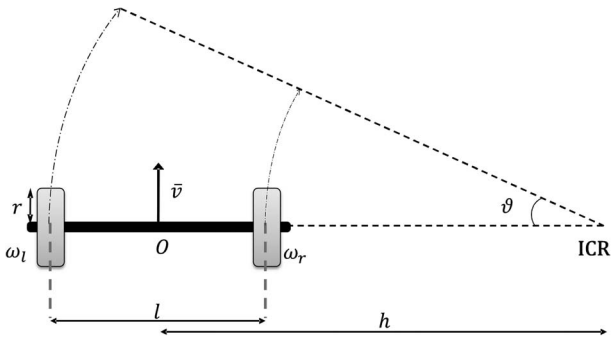

Fig. 7. Kinematic model of the differential drive.

III. Riding Commands

As mentioned in the previous section, the vehicle has two different ways to generate riding commands: by using the rider's weight distribution on the feet (in what follows, *feet riding mode*) and using a smartphone (*smartphone riding mode*). Both modes have three different options to be selected by the user, i.e., the *sport*, the *medium*, and the *soft*. The preceding options differ from one another, for instance, in the maximum and minimum longitudinal and steering speed values that the system is allowed to reach. The longitudinal speed command is always provided by the smartphone, whereas the steering one is provided either by the smartphone (in the *smartphone riding mode*) or by evaluating the load on each foot (in the *feet riding mode*). Specifically, in the latter case, the sum of the signals of the four pressure sensors is computed, and the result is low-pass filtered (with a cutoff frequency of 3 Hz, chosen so that it allows preserving the signal dynamics related to the required steering reaction time [16], [17]). Fig. 5 shows the steering commands obtained in the same maneuver with three different rider weights: 60, 70, and 100 kg. Note that, independent of the user's weight, left and right steering can be easily detected by simple zero-crossing monitoring. As can be seen, the steering commands are rescaled according to the thresholds of the current selected mode and represented in a range of $(-50, +50)$.

In the *smartphone riding mode*, instead, steering and speed commands are generated by tilting the smartphone so that the inertial sensors (accelerometers and gyroscopes) embedded in the device allow the identification of the different orientations. Specifically, based on the Android internal functions for sensor processing coupled with an active monitoring of the acceleration signals, it is possible to have an online estimate of its attitude angles. The active monitoring algorithm is used in order to monitor the outputs of the Android functions (which cannot be modified) and relies on ad hoc algorithms adapted from those described in [18] and developed to detect the attitude of a two-wheeled vehicle at low speed. Then, the longitudinal vehicle speed set point is determined according to the rotation about the vertical position of the smartphone (a pitch angle of 90°, corresponding to a vertical smartphone, which means that the desired speed is zero, whereas a pitch angle of 0°, corresponding to a horizontal smartphone, implies a request of the maximum longitudinal speed). Similarly, the steering speed set point is determined according to the rotation about the horizontal position of the smartphone (a 90° rotation clockwise means maximum steering speed to the right, whereas a 90° rotation anticlockwise means maximum steering speed to the left). Again, all commands (both those for longitudinal speed and steering speed) are rescaled between 0% and 100% (longitudinal speed) and between -50 and $+50$ (steering) and then sent to the motion control system, where they are appropriately converted into standard unity measures to be compatible with the physical controlled variables.

Fig. 6 shows the speed and steering commands of a smartphone-based riding session.

IV. Dynamical Vehicle Model

To model the vehicle dynamics of interest, let us start by considering the kinematic model of the differential drive, which is depicted in Fig. 7.

The vehicle motion can be described using the following two variables:

- the velocity $\bar{v}$, tangent to the vehicle trajectory and
- the angular velocity $\dot{\vartheta}$ due to the rotation around the *instantaneous center of rotation* (ICR).

The point O is the midpoint of the vehicle axis, whereas the constants included in the model are as follows:

- r, the driving wheels radius (assumed to be equal for both wheels);
- l, the length of the vehicle axis;
- h, the distance between O and the ICR.

Accordingly, $\overline{v}$ and $\dot{\vartheta}$ can be computed as

$$\begin{cases} \overline{v} = \frac{\omega_l + \omega_r}{2} r \\ \dot{\vartheta} = \frac{\omega_l - \omega_r}{l} r \end{cases} \tag{1}$$

where ω_l and ω_r are the rotational speed of the left and right driving wheels, respectively, which are the measured variables on board of the considered vehicle. Moreover, h can be expressed as

$$h = \frac{l}{2} \frac{\omega_l + \omega_r}{\omega_l - \omega_r}. \tag{2}$$

To derive a control-oriented model, it is worth recalling that the physical control inputs for the system are the two motor currents, which will be regulated with a dedicated servo control loop, whereas the controlled variables for managing the vehicle motion are selected (in accordance with the kinematic model introduced above) as

$$\begin{aligned} \overline{\omega} &= \frac{\omega_l + \omega_r}{2} = \frac{\overline{v}}{r} \\ \Delta\omega &= \omega_l - \omega_r = \dot{\vartheta} \frac{l}{r}. \end{aligned} \tag{3}$$

Thus, the variables $\overline{\omega}$ and $\Delta\omega$ in (3) represent (up to scaling factors) the *vehicle longitudinal speed* and the *steering speed*, the latter computed as the difference between the rotational speeds of the wheels.

Consistent with such a choice, the manipulated variables, i.e., the control inputs, are defined as

$$\begin{aligned} \bar{i} &= \frac{i^l_{\rm mot} + i^r_{\rm mot}}{2} \\ \Delta i &= i^l_{\rm mot} - i^r_{\rm mot} \end{aligned} \tag{4}$$

where $i^l_{\rm mot}$ and $i^r_{\rm mot}$ represent the input current of the left and right motors, respectively.

Once both manipulated and controlled variables have been defined, the input/output system dynamics can be described by the following multiple-input–multiple-output (MIMO) model:

$$\begin{bmatrix} \overline{\omega} \\ \Delta\omega \end{bmatrix} = \begin{bmatrix} G_{11}(s) & G_{12}(s) \\ G_{21}(s) & G_{22}(s) \end{bmatrix} \begin{bmatrix} \bar{i} \\ \Delta i \end{bmatrix} \tag{5}$$

where $G_{11}(s)$, $G_{12}(s)$, $G_{21}(s)$, and $G_{22}(s)$ are the transfer functions that describe the vehicle dynamics and will be detailed in the following.

To obtain an explicit model of the dynamics introduced in (5), one needs to describe the forces acting on the vehicle. To this aim, consider the schematic given in Fig. 8, where

- $J_{\rm rot}$ is the rotational inertia of the vehicle;
- $F_{\rm in}$ is the inertial force;
- F_c is the centrifugal force;
- F^l_y and F^r_y are the lateral forces acting on the left and right driving wheels, respectively;
- $F^{\rm front}_{\rm frict}$ and $F^{\rm rear}_{\rm frict}$ are the friction forces acting on the pivoting wheels;
- $F^l_{\rm frict}$ and $F^r_{\rm frict}$ are the friction forces acting on the left and right driving wheels, respectively;
- $F_{\rm drag}$ is the aerodynamic drag force acting on the vehicle;

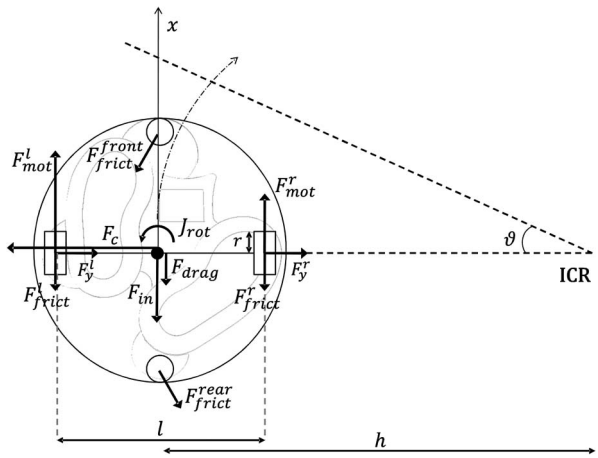

Fig. 8. Schematic of the forces acting on the considered vehicle.

- $F^l_{\rm mot}$ and $F^r_{\rm mot}$ are the traction forces provided by the electric motors;
- m_r is the mass of the rider;
- m_v is the mass of the vehicle;
- $M = m_v + m_r$.

The radii of the pivoting and driving wheels are assumed to be equal and are both indicated with r. To derive the description of the forces, the following are assumed to hold:

- the pivoting wheels can be modeled as spheres;
- the vehicle's chassis can be modeled as a disk;
- the center of mass is supposed to be coincident with the axis midpoint O.

Based on such assumptions, the vehicle is considered as a rigid body moving on a plane with three degrees of freedom (DOFs). Nevertheless, due to the limited rotational speed of the vehicle, the centrifugal forces are always balanced by the lateral friction forces, i.e.,

$$F_c = F^l_y + F^r_y. \tag{6}$$

Thus, as can be seen according to the kinematic model, the system has only two real DOFs, which will be those considered in what follows.

Before computing the force balance along the longitudinal axis and the torque balance around the center of mass O, all the friction forces acting on the system need to be characterized. Specifically, they can be divided into three components:

- rolling resistance

$$F_{\rm roll} = C_{\rm roll}\, Mg \tag{7}$$

- dynamic resistance

$$F_{\rm dyn}(\overline{v}) = \beta_{\rm dyn}\, \overline{v} \tag{8}$$

- drag forces

$$F_{\rm drag}(\overline{v}) = \frac{1}{2} \rho\, c_v A\, (\overline{v} + v_{\rm wind})^2 \tag{9}$$

where $\beta_{\rm dyn}$ is the dynamic resistance coefficient, $C_{\rm roll}$ is the rolling coefficient, ρ is the density of the air, and c_v is the drag coefficient, A is the reference front vehicle area and $v_{\rm wind}$ is

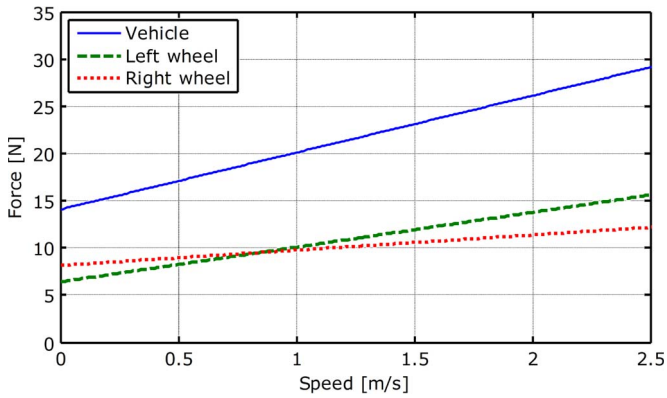

Fig. 9. Friction forces as a function of speed for left and right driving wheels and for the whole vehicle obtained in coasting down experiments.

TABLE II
COEFFICIENTS FROM COASTING DOWN FRICTION IDENTIFICATION

	Constant (C_{const})	Linear (C_{prop})
Vehicle	14.0749	6.0219
Left wheel	8.15	1.6096
Right wheel	6.3988	3.6823

the speed of the wind. In view of this description, the overall friction forces can be modeled as

$$F_{\text{frict}}(\overline{v}) = C_{\text{const}} + C_{\text{prop}}\,\overline{v} + C_{\text{quad}}\,\overline{v}^2. \tag{10}$$

However, considering that the maximum vehicle speed is approximately 10 km/h and that in indoor conditions one needs not account for the wind, the quadratic term in (10) can be omitted. This assumption is also supported by coasting down experiments carried out by letting the system (vehicle and rider) inertially decelerate from 10 km/h to zero. The relation between speed and friction forces experimentally obtained is reported in Fig. 9 for each driving wheel and for the whole vehicle, and the corresponding drag coefficients of the resulting linear model ($C_{\text{quad}} = 0$ in (10) for all tests) are listed in Table II.

Thus, the friction forces are computed as

$$F_{\text{frict}}(v) = C_{\text{prop}} v + C_{\text{cost}}. \tag{11}$$

Coasting down tests have been performed on both driving wheels, in order to highlight the nonidealities of the vehicle, which is, in principle, supposed to be symmetric. As can be noticed in Table II, $C^l_{\text{prop}} \neq C^r_{\text{prop}}$; thus, the friction forces for the two driving wheels are indeed different and can be expressed as

$$F^i_{\text{frict}}(\omega_i) = C^i_{\text{prop}}\omega_i r + C^i_{\text{cost}}, \quad i = l, r. \tag{12}$$

Being $C^r_{\text{prop}} > C^l_{\text{prop}}$ (see again Table II), the force balance along the x-axis takes the form

$$\begin{aligned} F^x_{\text{frict}}(\overline{v}) &= C^r_{\text{prop}}\omega_r r + C^l_{\text{prop}}\omega_l r \\ &= 2C^l_{\text{prop}}\overline{v} + \left(C^r_{\text{prop}} - C^l_{\text{prop}}\right)\omega_r r. \end{aligned} \tag{13}$$

Based on (3), ω_r can be rewritten as

$$\omega_r = \overline{\omega} + \frac{\Delta\omega}{2} \tag{14}$$

and substituting (14) into (13), one gets

$$\begin{aligned} F^x_{\text{frict}}(\overline{v}) = 2\left(C^l_{\text{prop}} + \left(C^r_{\text{prop}} - C^l_{\text{prop}}\right)\right)\overline{v} \\ + \left(C^r_{\text{prop}} - C^l_{\text{prop}}\right)\Delta v. \end{aligned} \tag{15}$$

To complete the vehicle motion description, the force balance along the longitudinal direction and the torque balance around the center of mass O must be computed. The force balance along the x-axis is given by

$$\sum F^x = F^x_{\text{in}} + F^x_{\text{frict}} - F^x_{\text{mot}} = 0 \tag{16}$$

where

$$F^x_{\text{in}} = \left(M + \frac{2J_d}{r^2} + \frac{J_{\text{mot}}\eta}{r^2 n^2} + 2J_{\text{rid}} + \frac{2J_{\text{pivot}}}{r^2}\right)\dot{\overline{\omega}} r \tag{17}$$

where

- J_{pivot} is the inertia of each pivoting wheel;
- η is the gearbox efficiency;
- n is the gearbox reduction ratio.

The forces provided by the two electric motors have the form

$$F^i_{\text{mot}} = \frac{T^i_{\text{mot}}\eta\, n}{r}, \quad i = l, r \tag{18}$$

where T^l_{mot} and T^r_{mot} are the torques generated by the left and right motors, respectively. Under the assumption that the two motors are identical and letting k be the torque constant, the motor forces can be computed as

$$F^x_{\text{mot}} = \frac{\eta n k}{r}\left(i^l_{\text{mot}} + i^r_{\text{mot}}\right) = \frac{2\eta n k}{r}\bar{i}. \tag{19}$$

Thus, (16) takes the form

$$\begin{aligned} &\left(M + \frac{2J_d}{r} + \frac{J_{\text{mot}}\eta}{r^2 n^2} + 2J_{\text{rid}} + \frac{2J_{\text{pivot}}}{r^2}\right)\dot{\overline{\omega}} r \\ &\quad + \left(C_{\text{prop}} + \left(C^r_{\text{prop}} - C^l_{\text{prop}}\right)\right)\overline{\omega} r \\ &\quad + \left(C^r_{\text{prop}} - C^l_{\text{prop}}\right)\Delta\omega r + C_{\text{cost}} - \frac{2k\bar{i}\eta n}{r} = 0. \end{aligned} \tag{20}$$

As M dominates all other summands in the first term of (20), the equation can be simplified as

$$\begin{aligned} &M\dot{\overline{\omega}} r - \left(2\,C^l_{\text{prop}} + \left(C^r_{\text{prop}} - C^l_{\text{prop}}\right)\right)\overline{\omega} r \\ &\qquad \times \frac{\left(C^r_{\text{prop}} - C^l_{\text{prop}}\right)}{2}\Delta\omega r + C_{\text{cost}} = \frac{2k\bar{i}\eta n}{r}. \end{aligned} \tag{21}$$

The torques involved in the torque balance around the center of mass of the vehicle are the inertial torque, the two equivalent torques generated by the driving forces, and the friction torques, thus yielding

$$\sum T^{(O)} = \sum T^{(O)}_{\text{in}} + \sum T^{(O)}_{\text{frict}} - \sum T^{(O)}_{\text{driving}} = 0. \tag{22}$$

The inertia torque $T^{(O)}_{\text{in}}$ is given by

$$\sum T^{(O)}_{\text{in}} = J_{\text{rot}}\ddot{\vartheta} \tag{23}$$

whereas, according to the sign convention adopted in Fig. 8, the driving torque $T^{(O)}_{\text{driving}}$ can be computed as

$$\begin{aligned}\sum T^{(O)}_{\text{driving}} &= \frac{l}{2}\left(F^l_{\text{mot}} - F^r_{\text{mot}}\right)\\ &= \frac{l}{2}\frac{\eta n k_t}{r}\left(i^l_{\text{mot}} - i^r_{\text{mot}}\right). \end{aligned} \tag{24}$$

Finally, considering (12), the friction torque $T^{(O)}_{\text{frict}}$ has the form

$$\begin{aligned}\sum T^{(O)}_{\text{frict}} &= \frac{l}{2}\left(F^l_{\text{frict}} - F^r_{\text{frict}}\right) + lF^{\text{pivot}}_{\text{frict}}\\ &= \frac{l}{2}\left(C^l_{\text{prop}}\omega_l r - C^r_{\text{prop}}\omega_r r + C^l_{\text{cost}} - C^r_{\text{cost}}\right)\\ &\quad + lc_{\text{pivot}}\overline{\omega} r\sin\vartheta. \end{aligned} \tag{25}$$

Note that, as $c_{\text{pivot}} \ll ((c^l_{\text{prop}} + c^r_{\text{prop}})/2)$ and ϑ is a small angle, the friction forces due to the pivoting wheels, in fact, can be neglected. Thus, (22) takes the form

$$\begin{aligned}J_{\text{rot}}\ddot{\vartheta} + \frac{l}{2}\left(C^l_{\text{prop}}\omega_l r - C^r_{\text{prop}}\omega_r r + C^l_{\text{cost}} - C^r_{\text{cost}}\right)\\ = \frac{l}{2}\frac{\eta n k_t}{r}\left(i^l_{\text{mot}} - i^r_{\text{mot}}\right). \end{aligned} \tag{26}$$

Furthermore, from (1), it follows that

$$\ddot{\vartheta} = \frac{r}{l}\Delta\dot{\omega}. \tag{27}$$

Thus, substituting (27) into (26), it yields

$$\begin{aligned}J_{\text{rot}}\frac{r}{l}\Delta\dot{\omega} + \frac{lr}{2}\left(C^l_{\text{prop}}\omega_l - C^r_{\text{prop}}\omega_r\right) + \frac{l}{2}\left(C^l_{\text{cost}} - C^r_{\text{cost}}\right)\\ = \frac{l}{2}\frac{\eta n k}{r}\Delta i. \end{aligned} \tag{28}$$

Recalling that (see Table II) $C^r_{\text{prop}} > C^l_{\text{prop}}$ and considering (14), (28) is rewritten as

$$\begin{aligned}J_{\text{rot}}\frac{r}{l}\Delta\dot{\omega} + \frac{lr}{2}\left(C^l_{\text{prop}} + \frac{C^r_{\text{prop}} - C^l_{\text{prop}}}{2}\right)\Delta\omega\\ - \frac{lr}{2}\left(C^r_{\text{prop}} - C^l_{\text{prop}}\right)\overline{\omega} + \frac{l}{2}\left(C^l_{\text{cost}} - C^r_{\text{cost}}\right)\\ = \frac{l}{2}\frac{\eta n k}{r}\Delta i. \end{aligned} \tag{29}$$

As such, the state equations of the vehicle dynamical model are given by

$$\begin{cases}\dot{\overline{\omega}} = -\frac{C^l_{\text{prop}}+C^r_{\text{prop}}}{m_{\text{tot}}}\overline{\omega} + \frac{C^r_{\text{prop}}-C^l_{\text{prop}}}{2m_{\text{tot}}}\Delta\omega + \frac{2k\eta n}{m_{\text{tot}}r^2}\bar{i}\\ \Delta\dot{\omega} = \frac{l^2\left(C^r_{\text{prop}}-C^l_{\text{prop}}\right)}{2J_{\text{rot}}}\overline{\omega} - \frac{l^2\left(C^l_{\text{prop}}+C^r_{\text{prop}}\right)}{4J_{\text{rot}}}\Delta\omega + \frac{l^2 n\eta k}{2J_{\text{rot}}r^2}\Delta i.\end{cases} \tag{30}$$

As can be noticed, (30) is a coupled MIMO system, for which the output equation is

$$y = \begin{bmatrix}y_1\\ y_2\end{bmatrix} = \begin{bmatrix}1 & 0\\ 0 & 1\end{bmatrix}\begin{bmatrix}\overline{\omega}\\ \Delta\omega\end{bmatrix}. \tag{31}$$

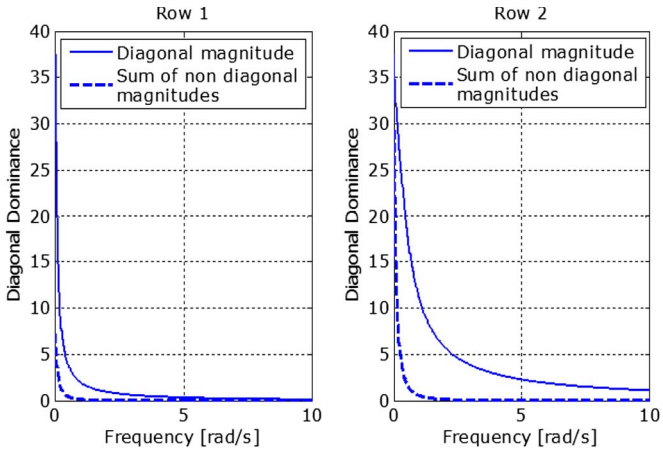

Fig. 10. Diagonal dominance as a function of the angular frequency for system (5).

To analyze the degree of coupling of the system, the transfer matrix (5) is considered, and a frequency-dependent version of the diagonal dominance measure is computed (see, e.g., [19]). Specifically, the diagonal dominance was evaluated for each row of the system matrix, and the results are depicted in Fig. 10 as a function of the angular frequency.

As a consequence, the system can be considered decoupled for all practical purposes, and the two friction coefficients for the left and right wheels can be assumed to be equal and expressed as

$$C_{\text{app}} = \frac{C^l_{\text{prop}} + C^r_{\text{prop}}}{2}. \tag{32}$$

Thus, the state equations of the decoupled MIMO system, which will be used for the vehicle motion controller design, have the form

$$\begin{cases}\dot{\overline{\omega}} = -\frac{C_{\text{prop}}}{m_{\text{tot}}}\overline{\omega} - \frac{C_{\text{cost}}}{m_{\text{tot}}r} + \frac{2k\eta n}{r^2 m_{\text{tot}}}\bar{i}\\ \Delta\dot{\omega} = -\frac{l^2 C_{\text{app}}}{2J_{\text{rot}}}\Delta\omega - \frac{l^2\left(C^l_{\text{cost}}-C^r_{\text{cost}}\right)}{2J_{\text{rot}}r} + \frac{l^2 k\eta n}{2J_{\text{rot}}r}\Delta i.\end{cases} \tag{33}$$

Then, the transfer matrix of the decoupled MIMO system is

$$G(s) = \begin{bmatrix}\frac{\mu_{11}}{\tau_{11}s+1} & 0\\ 0 & \frac{\mu_{22}}{\tau_{22}s+1}\end{bmatrix} \tag{34}$$

with

$$\tau_{11} = \frac{m_{\text{tot}}}{C_{\text{prop}}} \tag{35}$$

$$\mu_{11} = \frac{2k\eta n}{C_{\text{prop}}r^2} \tag{36}$$

$$\tau_{22} = \frac{4J_{\text{rot}}}{l^2\left(C^l_{\text{prop}} + C^r_{\text{prop}}\right)} \tag{37}$$

$$\mu_{22} = \frac{4k\eta n}{\left(C^l_{\text{prop}} + C^r_{\text{prop}}\right)r}. \tag{38}$$

The time constants τ_{11} and τ_{22} depend on the rider's mass, as $J_{\text{rot}} = J_{\text{rot}}(m_r)$. Apparently, the gains of the transfer function do not depend on the rider's mass; nevertheless, the friction coefficients are slightly affected by the rider's mass itself. In the following, for controller design, the nominal values of the rider's mass and of the friction coefficients will be used.

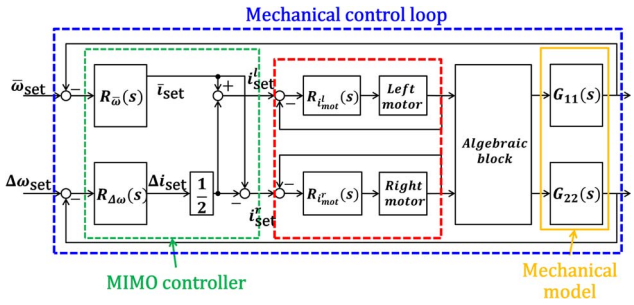

Fig. 11. Decoupled control layout for the considered vehicle.

V. Vehicle Motion Control

As depicted in Fig. 11, two control loops compose the vehicle motion control system: a servo controller for the motor currents and an external loop that regulates the vehicle speed and the steering speed as defined in (3). The electrical subsystem is composed of one current loop for each motor, and it is designed according to a cascade control scheme to ensure frequency decoupling with the mechanical outer loops.

The mechanical control loops are driven by the set points defined according to the riding commands described in Section III, which are translated into a desired vehicle speed set point $\overline{\omega}^*$ and a steering speed set point $\Delta\omega^*$ [see again (3)].

A. Electric Motors Servo Control

The inner loop depicted in Fig. 11 regulates the motors currents through a standard proportional–integral (PI) controller, using the PWM duty cycle as manipulated variable. The model considered for each dc motor is the equivalent RL circuit, which yields the well-known first-order transfer function model

$$G_m(s) = \frac{1}{R_{\text{mot}} + sL_{\text{mot}}} \tag{39}$$

where R_{mot} and L_{mot} are the motor equivalent resistance and inductance, respectively. The experimental step response of the system has been analyzed to identify the system parameters. Accordingly, two PI controllers have been tuned and implemented in antiwindup configuration, ensuring a loop cutoff frequency of 20 Hz. A frequency domain validation of the closed-loop system is shown in Fig. 12, which depicts the experimental complementary transfer function. Moreover, as for small values of the duty cycle, there is no current fluxing in the motors, thus yielding dead zone in the actuators; it has been necessary to design a feedforward action to avoid delays in the control loop. The final results achieved in a closed-loop step response are reported in Fig. 13.

B. Vehicle and Steering Speed Control

Consistent with what is shown in Fig. 11, the outer motion control loop is driven by the vehicle speed set point $\overline{\omega}^*$ and the steering speed set point $\Delta\omega^*$ defined by the user and employs the regulated motor currents [defined according to (4)] to control the speed and the lateral motion of the vehicle.

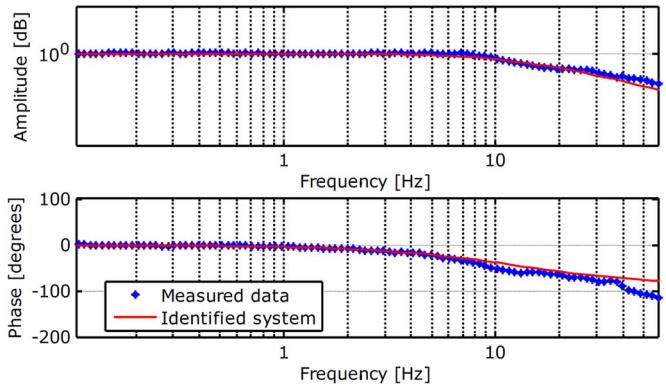

Fig. 12. Frequency domain validation of the closed-loop current control: (dots) measured data and estimated complementary transfer function model.

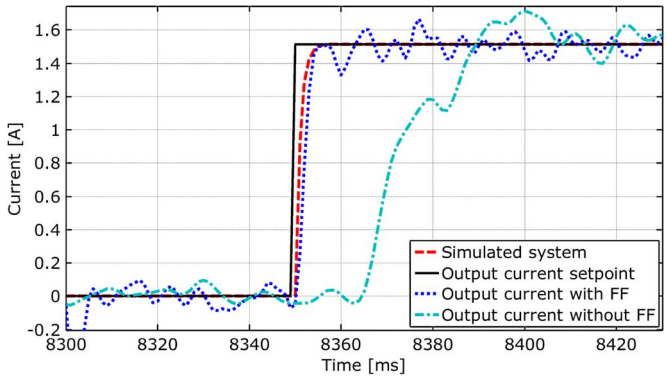

Fig. 13. Time histories of a closed-loop current step response (dotted line) with and (dash–dot line) without feedforward action.

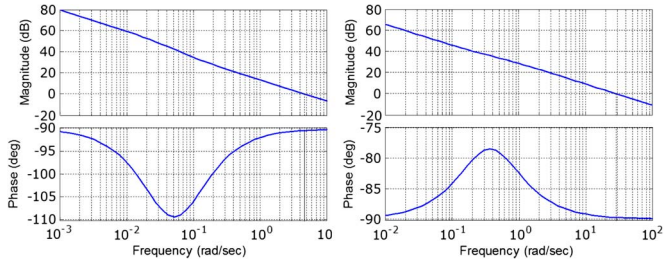

Fig. 14. (Left) Bode diagram of the loop transfer function for the longitudinal speed system. (Right) Bode diagram of the loop transfer function for the steering speed system.

In view of the results described in Section IV, the MIMO system that described the motion dynamics of interest is decoupled, and thus, the two control loops are separately designed. The cutoff frequencies of the two control loops have been selected to privilege a prompt response to the steering commands, which the user is most sensitive to. Accordingly, the cutoff frequency was set at 3 Hz for the steering dynamics and to 0.5 Hz for the longitudinal speed control loop [16], [17]. Fig. 14 shows the obtained loop transfer functions with the designed controllers.

1) Longitudinal Speed Controller: Recalling that the transfer function of interest (linking $\bar{\imath}$ to $\overline{\omega}$) is a linear first-order filter [see (33)], a PI controller in antiwindup configuration has been tuned in order to guarantee a closed-loop cutoff frequency of 0.5 Hz [20], [21].

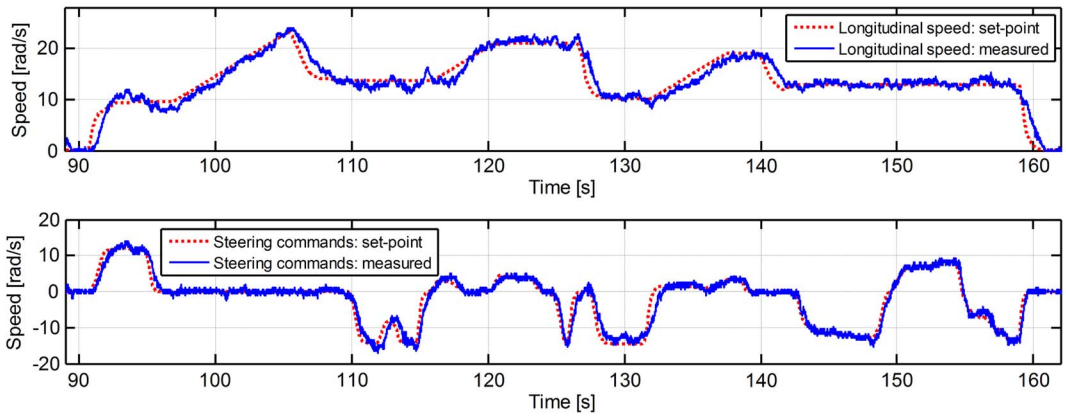

Fig. 15. Time histories of the closed-loop (top) longitudinal speed and (bottom) steering speed in a full riding session.

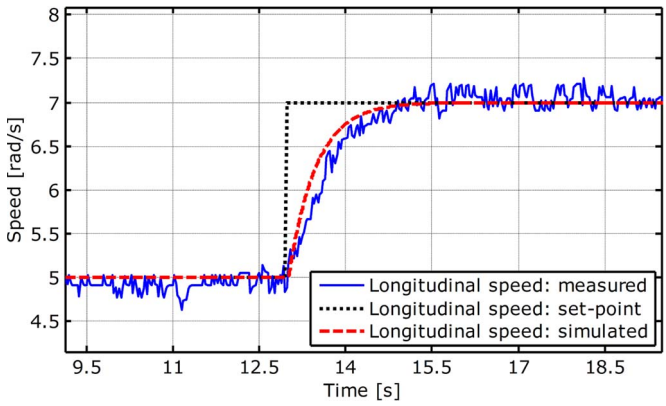

Fig. 16. Time histories of the closed-loop longitudinal speed $\overline{\omega}$ in an experimental step response test.

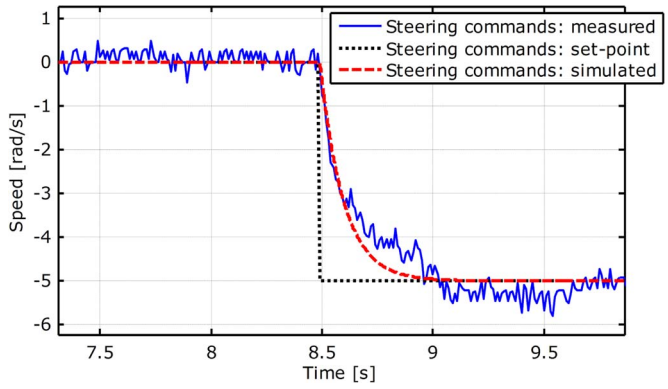

Fig. 17. Time histories of the closed-loop steering speed $\Delta\omega$ in an experimental test: right turn.

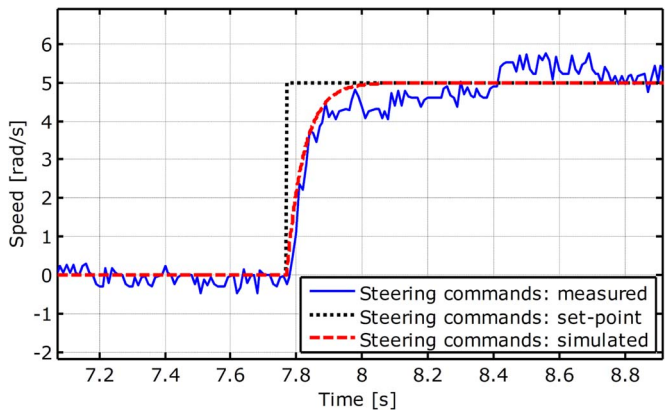

Fig. 18. Time histories of the closed-loop steering speed $\Delta\omega$ in an experimental test: left turn.

Again, experimental step responses have been employed to estimate the parameter values of the transfer function by generating equal current steps with both motors with a vehicle nominal load of 70 kg.

Based on these tests, the PI parameters have been selected, and the resulting closed-loop performance can be inspected in Figs. 15 and 16, which show that the system yields the desired performance. Note further that Fig. 16 also reports the results obtained with the simulation model based on (33): such results demonstrate that the proposed decoupled MIMO system fully captures the vehicle dynamics of interest and can thus be considered a reliable starting point for controller design.

2) Steering Speed Controller: Similar to what has been done for the longitudinal speed control, a linear and time invariant controller capable of guaranteeing a closed-loop cutoff frequency of 3 Hz has been tuned for regulating the steering speed of the vehicle. The resulting closed-loop performance can be inspected in Figs. 17 and 18, which show the experimental results obtained in a right and a left turn, respectively. Again, the vehicle behaves as expected and ensures symmetrical performance irrespectively of the steering direction. Once again, the consistency between the model and the real system is confirmed.

Finally, Fig. 15 shows the time histories of the two controlled variables, i.e., the longitudinal and steering speeds, obtained in a varied riding session, with a rider weighing 70 kg. As can be seen, the system ensures good tracking of the variables of interest, which results in a smooth path following and in a pleasant riding feeling.

C. Sensitivity Analysis

To analyze the robustness features of the proposed control system, a sensitivity analysis was carried out on the simulation model, which proved to be significantly consistent with the true vehicle dynamics. Furthermore, in order to confirm that the decoupling assumption that was used in the controller design

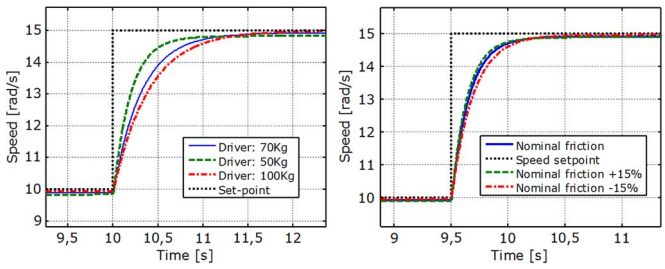

Fig. 19. Longitudinal speed control: sensitivity analysis on the full MIMO model with respect to the (left) rider's mass and to the (right) friction forces, which are the same on both wheels.

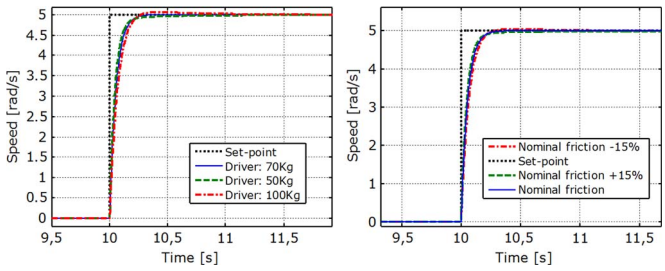

Fig. 20. Steering speed control: sensitivity analysis on the full MIMO model with respect to the (left) rider's mass and to the (right) friction forces, which are the same on both wheels.

actually holds, the whole sensitivity analysis is carried out using the full vehicle model.

Specifically, two parameters have varied, which account for most of the possible variations in the operating conditions: the rider's mass (which takes the values 50, 70, and 100 kg) and the coefficients that describe the friction forces (see Table II), which are varied by $\pm 15\%$ with respect to their nominal values.

The obtained results for the longitudinal speed control loop are shown in Fig. 19: as shown, the closed-loop system performance is not significantly affected by the variation of the considered parameters and the resulting closed-loop behavior maintains its desired features.

The same simulations have been carried out for the steering controller and the corresponding results are shown in Fig. 20: only very small performance variations are present and the performance can be regarded as satisfactory in all cases.

Furthermore, a simulation test with different friction forces applied to the two driving wheels was considered; the results are shown in Fig. 21: again, the performance can be regarded as satisfactory in all cases. Moreover, as the distance between the two driving wheels is quite small and the vehicle is designed for indoor usage, a working condition with different friction forces at the two wheels must be considered to be very uncommon.

VI. SSU

The riding posture is a critical safety aspect in the considered vehicle, as it does not provide handlebars, being thus sensitive to the rider's weight balance. This required the implementation of an SSU that manages hazardous driving situations.

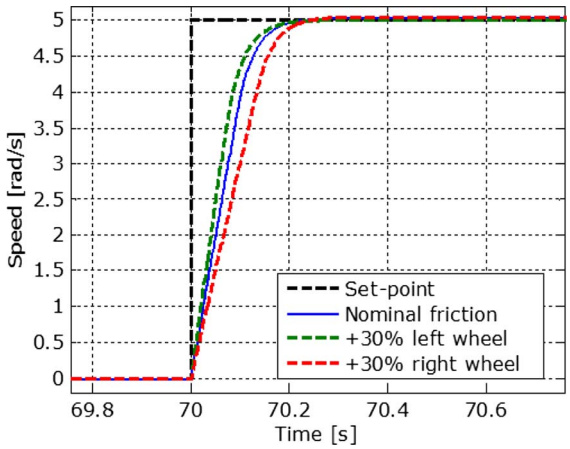

Fig. 21. Steering speed control: sensitivity analysis on the full MIMO model with different friction forces on the two driving wheels.

TABLE III
UPPER BOUNDS ON THE LONGITUDINAL ACCELERATION IN THE DIFFERENT RIDING MODES

Driving Mode	Max Acceleration	Max Deceleration
Soft	0.05 m/s^2	0.5 m/s^2
Medium	0.15 m/s^2	0.6 m/s^2
Sport	0.2 m/s^2	1 m/s^2

As shown in the overall control scheme outlined in Fig. 11, the SSU primarily acts as supervisor for the entire system by monitoring the state variables and modifying, if necessary, the user's commands. To detect a potential security hazard, the SSU analyzes in real time the longitudinal speed and acceleration, the Bluetooth connection status, and the pressure sensors measurements.

In particular, the SSU takes care of

- bounding the set point values and
- detecting when the user suddenly gets off the vehicle.

A. Set Point Limitation

To ensure the user balancing when the vehicle is in motion, the SSU takes care of supervising the set point values that come from both riding devices (smartphone and plantars). In particular, the limitations are set up on

- longitudinal acceleration and
- steering speed when the longitudinal speed is large.

1) Limitation on Longitudinal Acceleration: A different threshold on the longitudinal acceleration is defined for each of the three different driving modes implemented (see also Section III). Their values are reported in Table III.

2) Limitation of the Steering Speed: When the longitudinal speed is large, the steering speed generates significant centrifugal force, which causes discomfort to the rider and might be difficult to manage, causing potential hazards. Thus, the steering speed set point is limited by the SSU as a function of the longitudinal speed of the vehicle, as depicted in Fig. 22. As can be seen, the limitation is active for longitudinal speed values larger than 15 rad/s. An example of such a limitation in action during a riding session is reported in Fig. 23.

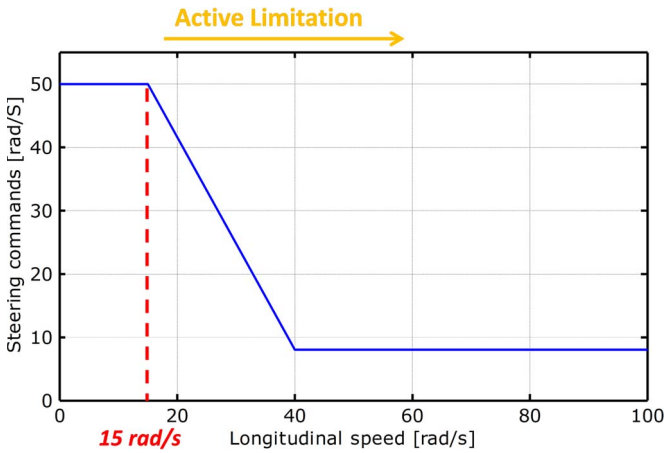

Fig. 22. Limitation of the steering speed set point $\Delta\omega^*$ as a function of the longitudinal speed.

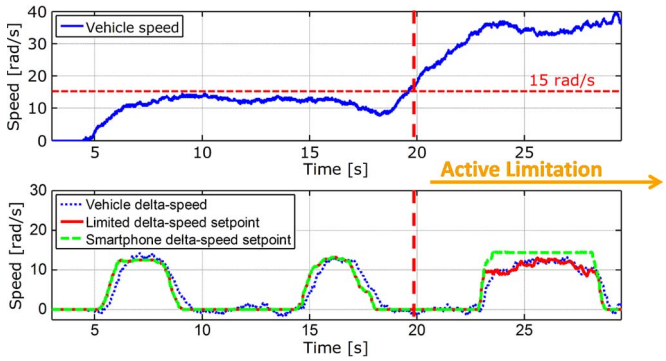

Fig. 23. Example of the actions of the SSU in limiting the value of the set point $\Delta\omega^*$ in a riding session.

B. Detection of the User Getting Off the Vehicle

If the user suddenly gets off the vehicle, the vehicle must immediately stop, for it not to be damaged or to hurt people nearby. In these situations, the SSU must detect the event by monitoring the sudden decrease in the pressure sensors measurements and set both the longitudinal and steering speed set points to zero. The event proved to be detectable by the SSU in less than 0.2 s, ensuring a fast and satisfactory reaction.

VII. Concluding Remarks and Outlook

In this paper, a novel electric vehicle for indoor mobility has been presented. Its main features are the absence of handlebars, which allow the user to have her/his hands free for attending the needed tasks, and a low power consumption due to its static stability that ensures a very good riding range, which is suitable for the needs of indoor environments. Furthermore, the combined design of the mechanical and electronic subsystems allowed us to realize a vehicle for which the motion control problem could be appropriately solved by means of linear and time invariant control systems, which proved to be robust in all working conditions. Finally, the user can drive the vehicle by balancing her/his feet on the given plantars and by using ad hoc applications developed for an Android-based smartphone platform equipped with inertial sensors. The performance of the closed-loop system has been analyzed in detail and proved to be appropriate, yielding an easy-to-ride vehicle that can be effectively employed by anyone right from the first attempt. Future work will address the design of personalization features, which will be based on autotuning procedures for the control system parameters that will be intended to provide adaptation to the single user's preferences and riding style. Additional safety facilities will be also considered, aimed to detect excessive slopes that can be dangerous for the vehicle's motion. Furthermore, for a public release of the vehicle, proximity-collision sensors will be employed for obstacle detection.

References

[1] H. G. Nguyen, J. Morrell, K. D. Mullens, A. B. Burmeister, S. Miles, N. Farrington, K. M. Thomas, and D. W. Gage, "Segway robotic mobility platform," in *Optics East*. Bellingham, WA, USA: SPIE, 2004, pp. 207–220.

[2] S. Savaresi, G. Alli, I. Boniolo, and C. Spelta, "Veicolo trasportatore," Italian Patent MI2010A 000 195, May 17, 2010.

[3] C. Spelta, I. Boniolo, G. Alli, S. Savaresi, and M. Vanzulli, "A planar electric vehicle with differential steering and a plantar command," in *Proc. IEEE Int. Conf. Control Appl.*, Denver, CO, USA, 2011, pp. 1457–1460.

[4] K. Li, T. Chen, Y. Luo, and J. Wang, "Intelligent environment-friendly vehicles: Concept and case studies," *IEEE Trans. Intell. Transp. Syst.*, vol. 13, no. 1, pp. 318–328, Mar. 2012.

[5] D. Ding, R. Cooper, S. Guo, and T. Corfman, "Analysis of driving backward in an electric-powered wheelchair," *IEEE Trans. Control Syst. Technol.*, vol. 12, no. 6, pp. 934–943, Nov. 2004.

[6] F. Grasser, A. D'Arrigo, S. Colombi, and A. Rufer, "Joe: A mobile inverted pendulum," *IEEE Trans. Ind. Electron.*, vol. 49, no. 1, pp. 107–114, Feb. 2002.

[7] A. Desai, D.-J. Lee, J. Moore, and Y.-P. Chang, "Stabilization and control of quad-rotor helicopter using a smartphone device," in *Proc. SPIE*, 2013, vol. 8662, pp. 866 208-1–866 208-9.

[8] M. Angermann, M. Frassl, and M. Lichtenstern, "Autonomous formation flying of micro aerial vehicles for communication relay chains," in *Proc. Nat. Tech. Meet.–Inst. Navig.*, 2011, pp. 1070–1076.

[9] I. Fantoni, R. Lozano, and M. W. Spong, "Energy based control of the Pendubot," *IEEE Trans. Autom. Control*, vol. 45, no. 4, pp. 725–729, Apr. 2000.

[10] S. Mirtaheri and S. Salimpoor, "HEV (hybrid electric vehicles) and the wiring reduction methods," in *Proc. IEEE Veh. Power Propulsion Conf.*, 2006, pp. 1–5.

[11] M. Conti, D. Fedeli, and M. Virgulti, "Bluetooth for electric vehicle to smart grid connection," in *Proc. Intell. Solutions Embedded Syst.*, 2011, vol. 1, pp. 13–18.

[12] A. Dardanelli, M. Tanelli, B. Picasso, S. Savaresi, O. di Tanna, and M. Santucci, "A smartphone-in-the-loop active state-of-charge manager for electric vehicles," *IEEE/ASME Trans. Mechatronics*, vol. 17, no. 3, pp. 454–463, Jun. 2012.

[13] M. Fazeen, B. Gozick, R. Dantu, M. Bhukhiya, and M. C. Gonzalez, "Safe driving using mobile phones," *IEEE Trans. Intell. Transp. Syst.*, vol. 13, no. 3, pp. 1462–1468, Sep. 2012.

[14] Y. Zhao, "Mobile phone location determination and its impact on intelligent transportation systems," *IEEE Trans. Intell. Transp. Syst.*, vol. 1, no. 1, pp. 55–64, Mar. 2000.

[15] J. D. Heinzmann and B. M. Taylor, The role of the Segway personal transporter (PT) in emissions reduction and energy efficiency, Segway Inc., Bedford, NH, USA. [Online]. Available: http://www.segway.com/downloads/pdfs/energy_efficient_segway_whitepaper.pdf

[16] H. Summala, "Drivers' steering reaction to a light stimulus on a dark road," *Ergonomics*, vol. 24, no. 2, pp. 125–131, Feb. 1981.

[17] H. Summala, "Driver/vehicle steering response latencies," *Hum. Factors*, vol. 23, no. 6, pp. 683–692, Dec. 1981.

[18] I. Boniolo and S. Savaresi, *Estimate of the Lean Angle of Motorcycles: Design and Analysis of Systems for Measuring and Estimating the Attitude Parameters of Motorcycles*. Saarbrücken, Germany: VDM Publishing, 2010.

[19] S. Skogestad and I. Postlethwaite, *Multivariable Feedback Control: Analysis and Design*. Hoboken, NJ, USA: Wiley, 2007.

[20] P. Hippe and C. Wurmthaler, "Systematic closed loop design in the presence of input saturation," *Automatica*, vol. 35, no. 4, pp. 689–655, Apr. 1999.

[21] Z. Z. Preitl, P. Bauer, and J. Bokor, "A simple control solution for traction motor used in hybrid vehicles," in *Proc. Appl. Comput. Intell. Inf.*, 2007, pp. 157–162.